scientific reports

Check for updates

OPEN

Waveform shaping in photonic time-crystals

Ruey-Bing Hwang

This paper reports on the waveform shaped by a finite duration photonic time-crystal with its permittivity and permeability periodically varying in time. A Gaussian-modulated sinusoidal pulse is incident onto this photonic time-crystal to evaluate the backward- and forward-scattering waveforms. An analytical formulation, utilizing a cascade of temporal transfer matrices and the inverse fast Fourier transform, was employed to conduct time-domain waveform computations. Interestingly, the dispersion diagram of the temporal unit cell, which displays a momentum gap characterized by a complex effective angular frequency, plays a crucial role in shaping the incident waveform. Specifically, the presence of momentum gaps in the spectrum of the incident pulse determines the frequencies of the generated oscillation modes.

The research on the propagation of electromagnetic waves in time-varying media can be traced back to Morgenthaler's 1958 paper[1]. Additionally, the observation of waves exhibiting exponentially increasing amplitudes, known as parametric amplification, within specific wave number ranges in a slab with time-modulated permittivity has been documented[2]. Extensive investigations have been conducted on the scattering characteristics of a plane wave interacting with a slab featuring time-periodic variations in permittivity or permeability[3–5]. Another area of study involves electromagnetic waves propagating in an infinite medium characterized by a traveling-wave modulation of sinusoidal form[6–8]. Additionally, the shape and spectrum of optical pulses can undergo transformations within a linear medium where the refractive index varies with time[9,10].

In a homogeneous and unbound medium, a sudden change in the permittivity and permeability over time throughout the entire space leads to the generation of reflected and transmitted waves within the same medium, attributed to the temporal interface. The continuity of the electric displacement field ($\mathbf{D}$) and magnetic field ($\mathbf{B}$) was applied at this interface, with constitutive relations $\mathbf{D}(t) = \varepsilon(t)\mathbf{E}(t)$ and $\mathbf{B}(t) = \mu(t)\mathbf{H}(t)$, in a linear non-dispersive medium[11]. It is noteworthy that the continuity of $\{\mathbf{E}, \mathbf{H}\}$ is unequivocal in dispersive medium such as rapidly growing plasma with $\mathbf{D} = \mathbf{E} + 4\pi \int_{-\infty}^{t} \chi(t, t')\mathbf{E}(t')dt'$[12].

Furthermore, the study encompassed an investigation into the reflection and transmission of electromagnetic waves at a temporal boundary, arising from an abrupt change in permittivity and permeability within an unbounded and homogeneous medium[13–15]. The research also delved into the examination of frequency-dependent reflection and transmission coefficients occurring at a temporal boundary within a dispersive medium[16].

To tailor the propagation properties of electromagnetic waves in materials, the time dimension has been introduced to design dynamic mediums or structures. This approach has been applied in various contexts, including engineering the frequency response of scattered fields from a temporal multilayer structure[17], designing antireflection coatings[18,19], synthesizing effective mediums[20,21], exploring temporal parity-time symmetry[22], investigating temporal Fabry-Perot cavities[23], studying photonic time crystals[24,25], analyzing spatiotemporal dielectric structures[26], developing quasisonic isolators[27], creating computational metamaterials[28–30], and constructing temporal photonic crystals made of dynamic transmission lines[31,32].

Notably, the photonic temporal crystals examined in this study differ from quantum time crystals, which address the concept of spontaneous time-translation symmetry breaking within quantum mechanics[33,34].

In this paper, the homogeneous and unbounded medium with abruptly changing in permittivity (refractive index) is considered. Specifically, the temporal variations are periodic with finite cycles (periods). The characteristic solutions, demonstrating the relationship between the effective angular frequency (ω_{eff}) and incident wave angular frequency, will be calculated. This relationship is crucial for predicting the output waveform when the incident wave spectrum is given. The excitation of modes within the complex ω_{eff} (or momentum gap) region significantly influences beam-shaping characteristics.

This paper is structured as follows. In the subsequent section, we will establish both the temporal input-output relation of electric and magnetic fields at a temporal interface, and the temporal transfer matrix representing the wave transition in a temporal slab. These foundational components will enable us to formulate the input-output

Institute of Communications Engineering, College of Electrical and Computer Engineering, National Yang Ming Chiao Tung University, Hsinchu 300093, Taiwan. email: raybeam@nycu.edu.tw

relation in a photonic time-crystal consisting of finite cycles (temporal slabs). In Section "Results and discussion", the forward (refracted) and backward (reflected) time-domain waveforms, along with their corresponding spectral responses, will be presented. Additionally, a table illustrating the Root Mean Square error between the outcomes of Finite Difference Time Domain simulation and the method developed in this paper is included. Finally, some concluding remarks on our findings will be provided in Section "Conclusion".

Methods

The transfer matrix method has been widely employed for analyzing wave scattering in scenarios that involve cascaded finite thickness uniform dielectric slabs[35–37]. In this section, we apply the temporal analog of the approach[17,19,38–41] to address the modulation of spatially homogeneous materials with time-varying permittivity $\varepsilon(t)$, permeability $\mu(t)$, or refractive index $n(t)$. Both $\varepsilon(t)$ and $\mu(t)$ undergo periodic changes with a period of $T_p = 1/f_p$, where f_p represents the pumping frequency of this dynamic medium. The homogeneous medium initially possesses parameters (μ_1, ε_1) during the first time segment lasting τ_1 seconds, followed by a second time segment with parameters (μ_2, ε_2) for a duration of τ_2 seconds.

Firstly, we will employ boundary conditions at a temporal interface to establish an input-output relation for the electric and magnetic fields, expressed in terms of a 2-by-2 matrix denoted as the junction matrix. Additionally, we will derive the transition of electric and magnetic fields within a temporal slab to determine a 2-by-2 transfer matrix. Given that the medium undergoes multiple cycles of changes, one can determine the backward- and forward-scattering waveforms at the steady state of a photonic time-crystal by cascading multiple temporal transfer and junction matrices together.

Wave scattering at a temporal interface

Consider a monochromatic plane wave traveling in an homogeneous, isotropic, non-dispersive, and unbounded medium; however, the medium is time varying. Its permittivity ε and permeability μ can be abruptly switched from (μ_1, ε_1) to (μ_2, ε_2) at $t = t_o$. In a uniform medium, the electric and magnetic fields can be expressed as $E_x(z,t) = E_1 \exp(ikz - i\omega_1 t)$ and $H_y(z,t) = H_1 \exp(ikz - i\omega_1 t)$, respectively. Parameters ω_1 is the angular frequency in the initial state and k is the wavenumber. The field amplitudes satisfy $Z_1 = E_1/H_1$ and $Z_1 = \sqrt{\mu_1/\varepsilon_1}$. After the switching event the fields become

$$E_x(z, t > t_o) = \left[Fe^{-i\omega_2(t-t_o)} + Be^{i\omega_2(t-t_o)}\right] E_1 e^{i(k_2 z - \omega_1 t_o)}, \tag{1}$$

$$H_y(z, t > t_o) = Y_2\left[Fe^{-i\omega_2(t-t_o)} - Be^{i\omega_2(t-t_o)}\right] E_1 e^{i(k_2 z - \omega_1 t_o)}. \tag{2}$$

Parameters F and B represent the forward scattering (or transmission) and backward scattering (or reflection) coefficients, respectively. $Z_2 = 1/Y_2 = \sqrt{\mu_2/\varepsilon_2}$ is the wave impedance after the switching event. The temporal boundary conditions, $\mathbf{D}(t = t_o^-) = \mathbf{D}(t = t_o^+)$ and $\mathbf{B}(t = t_o^-) = \mathbf{B}(t = t_o^+)$, must be satisfied everywhere in space, leading to $k = k_2$ or $\omega_1\sqrt{\mu_1\varepsilon_1} = \omega_2\sqrt{\mu_2\varepsilon_2}$. This implies momentum conservation across the temporal interface.

The temporal boundary conditions facilitate the formulation of two equations: $\varepsilon_1 E_x(z, t = t_o^-) = \varepsilon_2 E_x(z, t = t_o^+)$ and $\mu_1 H_y(z, t = t_o^-) = \mu_2 H_y(z, t = t_o^+)$, which can be expressed in a matrix-vector form as follows.

$$\begin{bmatrix} E_x(z, t_o^+) \\ H_y(z, t_o^+) \end{bmatrix} = \begin{bmatrix} \varepsilon_1/\varepsilon_2 & 0 \\ 0 & \mu_1/\mu_2 \end{bmatrix} \begin{bmatrix} E_x(z, t_o^-) \\ H_y(z, t_o^-) \end{bmatrix} \tag{3}$$

Equation (3) defines the input-output relation of the electric and magnetic fields at the temporal interface.

Transfer matrix in a temporal slab

Consider a wave propagating within a temporal slab characterized by a time interval denoted as τ. For instance, the time interval is $t \in (t_o^+, t_o + \tau)$ in Eqs. (1) and (2). The electric and magnetic fields at $t = t_o^+$ can be written as $E_x(z, t = t_o^+) = (F + B)E_1 e^{i(k_2 z - \omega_1 t_o)}$ and $H_y(z, t = t_o^+) = Y_2(F - B)E_1 e^{i(k_2 z - \omega_1 t_o)}$. Therefore, the forward scattering coefficient F and backward scattering coefficient B can be expressed in terms of $E_x(z, t = t_o^+)$ and $H_y(z, t = t_o^+)$. Substituting the obtained F and B into Eqs. (1) and (2) at $t = t_o + \tau$, the electric and magnetic fields evaluated at $t = t_o + \tau$ can be expressed in terms of those at $t = t_o^+$ and written in the temporal transfer matrix given below.

$$\begin{bmatrix} E_x(z, t_o + \tau) \\ H_y(z, t_o + \tau) \end{bmatrix} = \begin{bmatrix} \cos\omega_2\tau & -iZ_2 \sin\omega_2\tau \\ -iY_2 \sin\omega_2\tau & \cos\omega_2\tau \end{bmatrix} \begin{bmatrix} E_x(z, t_o^+) \\ H_y(z, t_o^+) \end{bmatrix} \tag{4}$$

Notably, the result provided by Eq. (4) can be extended to any temporal slab characterized by $(\mu_i,\ \varepsilon_i)$, provided that the angular frequency of the wave satisfies $\omega_i\sqrt{\mu_i\varepsilon_i} = k$, where k represents the momentum in the initial state.

A finite cascade of temporal slabs

In an unbounded and homogeneous medium, a periodically time-varying scenario emerges where the permeability and permittivity alternate cyclically between (μ_1, ε_1) and (μ_2, ε_2) with dwell time of τ_1 and τ_2, respectively. The permittivity and permeability (or refractive index) of the medium undergo periodic variations over time, transitioning between these two specified states. For instance, as depicted in Fig. 1, the system comprises four

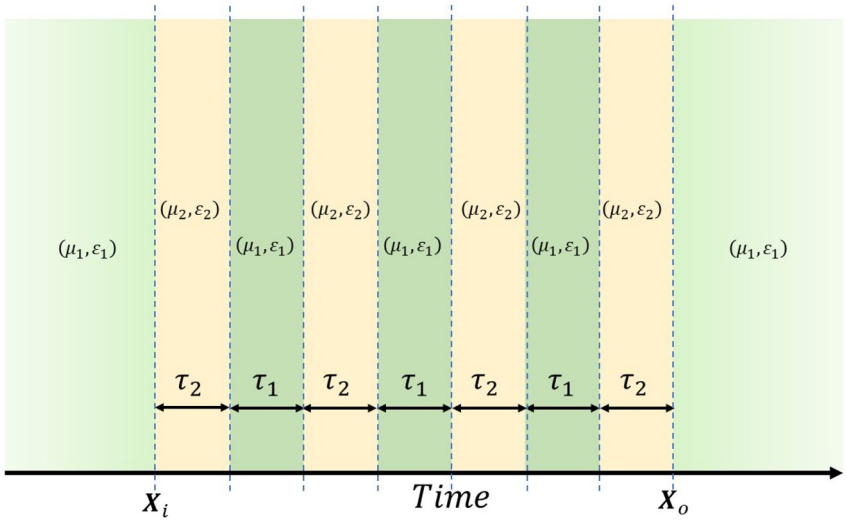

Figure 1. Variation of permeability and permittivity of the temporal photonic crystal against time: it consists of 4 states of (μ_2, ε_2) and three states of (μ_1, ε_1) in the transition region between $\mathbf{X_o}$ and $\mathbf{X_i}$. The time duration within each temporal slab is denoted as τ_1 and τ_2.

states with parameters (μ_2, ε_2) and three states with parameters (μ_1, ε_1) within the transition region between $\mathbf{X}_i$ and $\mathbf{X}_o$.

The comprehensive input-output relation of E_x and H_y can be derived by sequentially combining those of the constituent components, which encompass the temporal transfer matrix described in Eq. (4) and the junction continuity at the temporal interface outlined in Eq. (3), as elucidated in the preceding sections. This yields the subsequent expression:

$$\mathbf{X}_o = \mathbf{C}_{12}\mathbf{T}_2\mathbf{C}_{21}\mathbf{T}_1\mathbf{C}_{12}\mathbf{T}_2\mathbf{C}_{21}\mathbf{T}_1\mathbf{C}_{12}\mathbf{T}_2\mathbf{C}_{21}\mathbf{T}_1\mathbf{C}_{12}\mathbf{T}_2\mathbf{C}_{21}\mathbf{X}_i \tag{5}$$

with

$$\mathbf{C}_{ij} = \begin{bmatrix} \varepsilon_j/\varepsilon_i & 0 \\ 0 & \mu_j/\mu_i \end{bmatrix}, \tag{6}$$

Here, the matrix $\mathbf{C}_{ij}$ is referred to as the junction matrix at the temporal interface between the i-th and j-th segments (temporal slab).

$$\mathbf{T}_j = \begin{bmatrix} \cos\omega_j T_j & -iZ_j \sin\omega_j T_j \\ -iY_j \sin\omega_j T_j & \cos\omega_j T_j \end{bmatrix} \tag{7}$$

where the matrix $\mathbf{T}_j$ is termed as the temporal transfer matrix in the jth time segment.

Where $\mathbf{X}_o = [E_x(t_o + T_e)\ H_y(t_o + T_e)]^T$, $\mathbf{X}_i = [E_x(t_o^-)\ H_y(t_o^-)]^T$ and $T_e = 4(\tau_1 + \tau_2) - \tau_1$ represents the total time for cycles. The parameter $Z_j = \sqrt{\mu_j/\varepsilon_j}$ corresponds to the wave impedance in the jth temporal slab, where j=1 or 2.

Due to momentum conservation, the continuity in k between the two states implies that $k = \omega_1\sqrt{\mu_1\varepsilon_1} = \omega_2\sqrt{\mu_2\varepsilon_2}$. This relationship allows us to determine the angular frequency in medium 2 (ω_2) given the angular frequency in medium 1 (ω_1), expressed as $\omega_2 = \omega_1\sqrt{\frac{\mu_1\varepsilon_1}{\mu_2\varepsilon_2}}$.

In reality, the aforementioned system comprises three complete cycles (time periods) and one incomplete cycle. However, we can represent it as four cycles and multiply it with $\mathbf{T}_1^{-1}$, as shown below:

$$\mathbf{X}_o = \mathbf{T}_1^{-1}\underbrace{\mathbf{T}_1\mathbf{C}_{12}\mathbf{T}_2\mathbf{C}_{21}}_{\mathbf{U}}\underbrace{\mathbf{T}_1\mathbf{C}_{12}\mathbf{T}_2\mathbf{C}_{21}}_{\mathbf{U}}\underbrace{\mathbf{T}_1\mathbf{C}_{12}\mathbf{T}_2\mathbf{C}_{21}}_{\mathbf{U}}\underbrace{\mathbf{T}_1\mathbf{C}_{12}\mathbf{T}_2\mathbf{C}_{21}}_{\mathbf{U}}\mathbf{X}_i \tag{8}$$

with

$$\mathbf{U} = \mathbf{T}_1\mathbf{C}_{12}\mathbf{T}_2\mathbf{C}_{21} \tag{9}$$

In this expression, $\mathbf{U}$ represents the temporal transfer matrix of the unit cell, which comprises two junction matrices and two temporal transfer matrices.

Following this principle, we can extend the approach to a scenario with N_c incomplete cycles, comprising N_c temporal slab 2 and $N_c - 1$ temporal slab 1. As a result, the input-output relation of the column vector consisting of E_x and H_y can be formulated as follows:

$$\mathbf{X}_o = \mathbf{T}_1^{-1}\mathbf{U}^{N_c}\mathbf{X}_i \tag{10}$$

Based on the theory of eigendecomposition, matrix $\mathbf{U}$ can be factorized as $\mathbf{U} = \mathbf{PDP}^{-1}$.

Where $\mathbf{P}$ is a matrix whose columns are the eigenvectors of $\mathbf{U}$, and $\mathbf{D}$ is a diagonal matrix whose entries of λ_1 and λ_2 are the corresponding eigenvalues of $\mathbf{U}$. Eigendecomposition allows us to simplify and analyze the properties of $\mathbf{U}$ in terms of its eigenvectors and eigenvalues, making it easier to understand the system's behavior.

Therefore, Eq. (10) can be rewritten as follows.

$$\mathbf{X}_o = \mathbf{T}_1^{-1}\mathbf{P}\mathbf{D}^{N_c}\mathbf{P}^{-1}\mathbf{X}_i, \tag{11}$$

with

$$\mathbf{D}^{N_c} = \begin{bmatrix} \lambda_1^{N_c} & 0 \\ 0 & \lambda_2^{N_c} \end{bmatrix}. \tag{12}$$

This expression substantially reduces the computational complexity involved in calculating the system's transfer matrix in Eq. (5).

The E_x and H_y in the steady state of the crystal end with parameters (μ_1, ε_1) are expressed as follows:

$$E_x(z,t) = \left[Fe^{-i\omega_1(t-t_o-T_e)} + Be^{+i\omega_1(t-t_o-T_e)}\right]e^{ikz}, \tag{13}$$

and

$$H_y(z,t) = Y_1\left[Fe^{-i\omega_1(t-t_o-T_e)} - Be^{+i\omega_1(t-t_o-T_e)}\right]e^{ikz} \tag{14}$$

where $t \geq t_o + T_e$ and $T_e = N_c(\tau_1 + \tau_2) - \tau_1$ is the temporal length of the time-crystal.

If we define that

$$\mathbf{T}_1^{-1}\mathbf{P}\mathbf{D}^{N_c}\mathbf{P}^{-1} := \begin{bmatrix} t_{11} & t_{12} \\ t_{21} & t_{22} \end{bmatrix} \tag{15}$$

By substituting Eqs. (13), (14) and (15) into Eq. (11), one can determine the forward- and backward-wave amplitudes, shown below.

$$F = \frac{1}{2}(t_{11} + t_{12}Y_1 + t_{21}Z_1 + t_{22})E_1e^{-i\omega_1 t_o}, \tag{16}$$

and

$$B = \frac{1}{2}(t_{11} + t_{12}Y_1 - t_{21}Z_1 - t_{22})E_1e^{-i\omega_1 t_o}. \tag{17}$$

Given that the incident wave can consist of a continuous spectrum, the voltage E_1 becomes a function of the incident wave's angular frequency, denoted as $E_1(\omega_1)$. The system's response in terms of the forward and backward wave amplitudes will be linked to the spectral function of the incident wave. This perspective enables us to understand the time-domain waveforms of the forward and backward waves under an arbitrary incident waveform, rather than solely focusing on realizing the impulse response of the system.

In this research, a Gaussian-modulated sinusoidal pulse with the spectral function given below is employed as the excitation source (or incident waveform).

$$E_1(\omega_1) = \frac{\sigma\sqrt{2\pi}}{2i}\exp(-i\omega_1\gamma)\left[\exp(-\frac{\sigma^2(\omega_1-\omega_c)^2}{2}) - \left[\exp(-\frac{\sigma^2(\omega_1+\omega_c)^2}{2})\right]\right]. \tag{18}$$

Its corresponding time-domain waveform is

$$E_1(t) = \exp\left[-\frac{(t-\gamma)^2}{2\sigma^2}\right]\sin\omega_c(t-\gamma). \tag{19}$$

where σ, ω_c and γ are the pulse width, carrier frequency and offset time of the modulated Gaussian pulse, respectively. It is important to note that a larger bandwidth results in a narrower time pulse width.

Specifically, the forward and backward scattering waveforms can be efficiently computed through the spectral functions of F and B using the commonly used (IFFT) inverse fast Fourier transform algorithm.

Complex ω_{eff} inside the momentum gap

As mentioned previously, the transfer matrix of the unit cell $\mathbf{U}$ has two eigenvalues denoted as λ_1 and λ_2. These eigenvalues satisfy the following two equations:

$$\lambda_1 + \lambda_2 = \mathrm{trace}(\mathbf{U}), \tag{20}$$

$$\lambda_1\lambda_2 = \det(\mathbf{U}) = \det(\mathbf{T}_1)\det(\mathbf{C}_{12})\det(\mathbf{T}_2)\det(\mathbf{C}_{21}) = 1. \tag{21}$$

where the symbol "trace" represents the trace of a matrix, which is the sum of its diagonal elements. Furthermore, it is known that $\det(\mathbf{C}12)\det(\mathbf{C}21) = 1$, $\det(\mathbf{T}_1) = 1$, and $\det(\mathbf{T}_2) = 1$.

Since $\lambda_1\lambda_2 = 1$, it allows us to set the eigenvalues (λ) equal to $\exp(\pm i\omega_{\text{eff}}T_p)$, where ω_{eff} represents the effective angular frequency of the unit cell and $T_p = \tau_1 + \tau_2$ is the cycle time (time period), and $f_p = 1/T_p$ can be interpreted as the pumping frequency of the photonic time crystal (dynamic medium). Now, Eq. (20) can be explicitly written as follows.

$$\cos(\omega_{\text{eff}}T_p) = \cos\omega_1\tau_1\cos\omega_2\tau_2 - Q\sin\omega_1\tau_1\sin\omega_2\tau_2 \tag{22}$$

with $Q = \frac{1}{2}(Z_1/Z_2 + Z_2/Z_1)$.

From Eq. (22), we know that ω_{eff} becomes a complex number once the absolute value of the right-hand side term is greater than one. This phenomenon is known as the momentum gap, as reported in the literature. Within the momentum gap, the effective angular frequency is a complex number, and the two eigenvalues are $\exp[\pm i(\omega_r + i\omega_i)T_p]$, where ω_r and ω_i are the real and imaginary parts of ω_{eff}. Due to the relationship $\lambda_1\lambda_2 = 1$, when one eigenvalue has an amplitude less than one and exhibits exponential decay, the other one has an amplitude greater than one and demonstrates exponential growth.

Notably, the input-output relation in Eq. (11) is related to $\lambda_1^{N_c}$ and $\lambda_2^{N_c}$. These two parameters play an important role in amplitude amplification, known as parametric amplification[42,43], particularly for the eigenvalue associated with exponential growth. This increase in energy is provided by the pumping energy of the dynamic medium. Accordingly, an increase in N_c enhances the output signal strength, as will be observed in the numerical results.

Results and discussion

In this section, we explore a photonic time crystal with a periodically changing refractive index over time. This medium exhibits two temporal states of refractive index: $n_1 = 1.55$ with a dwell time τ_1 and $n_2 = 1.79$ with a dwell time τ_2. Here, we set $\tau_1 = \tau_2$, resulting in a duty cycle of 50 percent. It's worth noting that in all the simulation results, time is normalized to T_p, and angular frequency is normalized to ω_p.

The incident wave is a Gaussian-modulated sinusoidal pulse with a carrier frequency ω_c and a bandwidth ranging from $\omega_c - d\omega$ to $\omega_c + d\omega$. The values of ω_c and $d\omega$ are separately provided in various examples.

Prior to undertaking the detailed waveform analysis, we initially computed the characteristic solution, denoted as ω_{eff}, from the transfer matrix of the unit cell, as defined in Eq. (22). This preliminary step proved crucial in comprehending the system's behavior, given that the unit cell transfer matrix functions as the fundamental building block of the entire system.

Figure 2 depicts the correlation between the effective angular frequency (ω_{eff}) and ω_1 (incident wave angular frequency). The blue and red curves represent the real and imaginary components of $\omega_{\text{eff}}/\omega_p$, respectively. Distinct bump-like shapes are clearly observable in the curves, particularly in the momentum gap regions. This phenomenon bears similarity to the behavior exhibited by the imaginary part of the propagation constant within the bandgap of a spatial photonic crystal.

The physical interpretation of ω_{eff} lies in its role as the effective or average angular frequency of the wave propagating in the temporal unit cell, analogous to the concept of an effective propagation constant in spatial crystals. While the majority of ω_{eff} values are real, there are specific regions where they become complex. This suggests the coexistence of both exponential growth and decay of eigenvalues (λ). Notably, the exponential

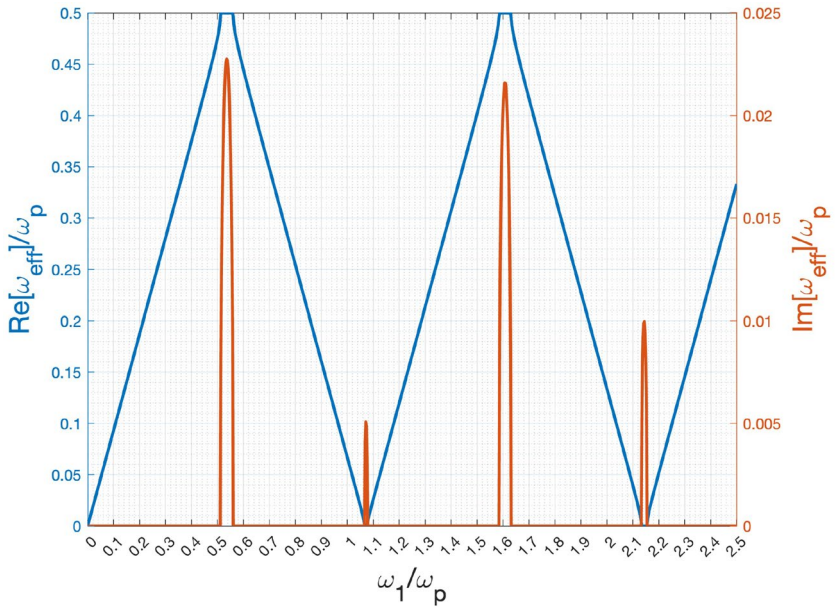

Figure 2. Relationship between normalized effective angular frequency ($\omega_{\text{eff}}/\omega_p$) against the incident wave angular frequency of ω_1 normalized to ω_p: the refractive indices of the two state respectively are $n_1 = 1.55$, $n_2 = 1.79$; the time duration of the two states are $\tau_1 = \tau_2$. Parameter $\omega_p = 2\pi/(\tau_1 + \tau_2)$ is the pumping angular frequency of the dynamic medium.

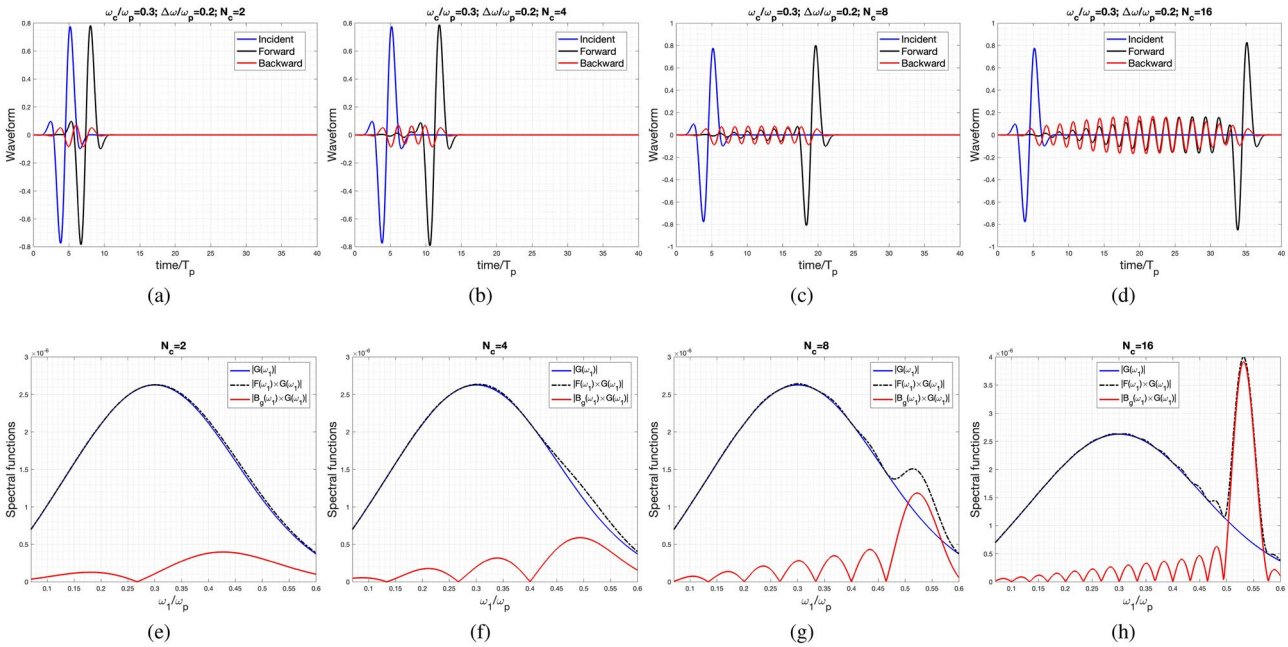

Figure 3. Incident, reflected and transmitted waveform for the case of $\omega_c/\omega_p = 0.3$, $d\omega/\omega_p = 0.2$ for various cycles: (**a**) $N_c = 2$, (**b**) $N_c = 4$, (**c**) $N_c = 8$, and (**d**) $N_c = 16$. Spectral functions of the Incident, reflected and transmitted waves corresponding to the previous waveform for various cycles; where $G(\omega_1)$ is the spectral function of the incident wave. Each sub-figure has the number of cycles of: (**e**) $N_c = 2$, (**f**) $N_c = 4$, (**g**) $N_c = 8$, and (**h**) $N_c = 16$.

growth component significantly contributes to the amplification of an input signal, a point that will be further elucidated in subsequent discussions.

Figure 3 presents the incident, reflected, and transmitted waveforms plotted against time, normalized to T_p. The chosen time range ensures a clear observation of the complete waveform. The center frequency is $\omega_c/\omega_P = 0.3$, where ω_{eff} is a real number (refer to Fig. 2). However, the signal bandwidth ($d\omega/\omega_p = 0.2$) covers the first momentum gap.

In Fig. 3a, it is evident that the forward waveform closely resembles the incident wave, while the backward wave experiences a significant reduction in amplitude. As the number of cycles (N_c) increases (from Fig. 3b–d), the forward wave continues to closely mimic the incident wave. However, its oscillating tail becomes more pronounced and extends further with the increase in N_c.

Figures from Fig. 3e–h depict the spectral functions of incident, backward, and forward waves corresponding to each case in Figures from Fig. 3a–d. Notably, the spectral function of the incident wave is denoted as $G(\omega_1)$, and both the backward and forward wave spectral functions are multiplied by $G(\omega_1)$.

In Fig. 3e, it is observed that the forward-wave spectral function closely mirrors that of the incident wave, explaining the similarity in their waveforms shown in Fig. 3a. As N_c increases, a noticeable discrepancy between the incident- and forward-wave spectral functions emerges, particularly around the first momentum gap with complex ω_{eff}. This difference arises due to the excitation of the exponential growth mode, allowing the presence of another Gaussian-modulated sinusoidal pulse with a wider pulse width (due to a narrower bandwidth spectrum in the first momentum gap), as depicted in Fig. 3c and d. Moreover, in Fig. 3h, a narrow-band Gaussian-modulated pulse centered around $\omega_c/\omega_p = 0.55$ is superimposed onto the incident-wave spectral function. This corresponds to the wide Gaussian-modulated pulse accompanying the incident pulse, as illustrated in Fig. 3d.

On the other hand, the reflected wave spectral function is dominated by the complex ω_{eff} mode, resulting in the appearance of only the wide pulse-width Gaussian-modulated pulse.

In the following example, the central frequency of the incident wave is set to $\omega_c/\omega_p = 0.543$, strategically positioned at the center of the first momentum gap. This configuration is characterized by a narrow bandwidth of $d\omega/\omega_p = 0.05$. From Fig. 4a, it can be observed that the difference between the incident and forward waveforms appears to be insignificant, except for a slight amplitude amplification. The amplitude amplification for the forward wave is evident while the shape of the waveform remains, as depicted in Fig. 4b with $N_c = 4$.

In contrast, the two cases with $N_c = 8$ and $N_c = 16$, illustrated in Fig. 4c and d, reveal a substantial discrepancy between the incident and forward/backward waveforms. In these instances, the carrier frequency remains constant, while the pulse width broadens for both forward and backward waveforms. This observation is supported by their corresponding spectral functions depicted in Fig. 4g and h.

Specifically, in Fig. 4h, an additional narrower Gaussian pulse, originating from the first momentum gap, overlays the incident pulse, aligning their central frequencies. Therefore, it becomes apparent that the pulse width is predominantly determined by the narrow-band component, while maintaining the same central frequency.

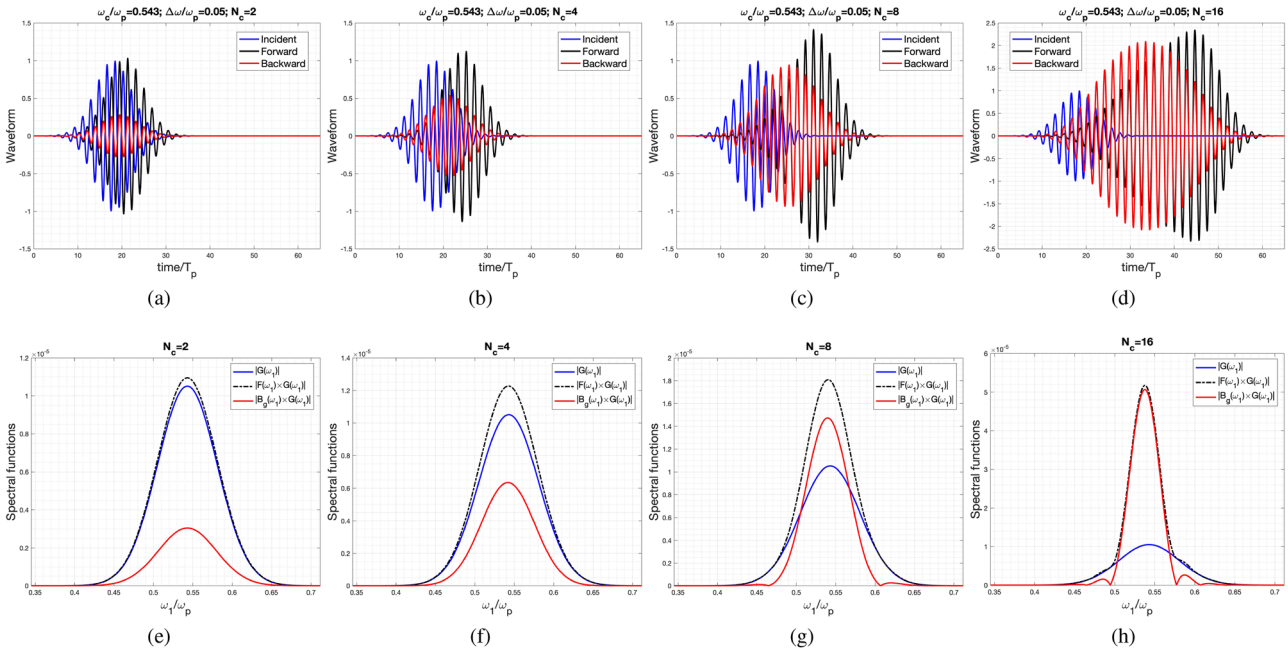

Figure 4. Incident, reflected and transmitted waveform for the case of $\omega_c/\omega_p = 0.543$, $d\omega/\omega_p = 0.05$ for various cycles: (**a**) $N_c = 2$, (**b**) $N_c = 4$, (**c**) $N_c = 8$, and (**d**) $N_c = 16$. Spectral functions of the Incident, reflected and transmitted waves corresponding to the previous waveform for various cycles; where $G(\omega_1)$ is the spectral function of the incident wave. Each sub-figure has the number of cycles of: (**e**) $N_c = 2$, (**f**) $N_c = 4$, (**g**) $N_c = 8$, and (**h**) $N_c = 16$.

Additionally, the backward wave exhibits a wider pulse width, a consequence of the narrow-band spectrum displayed in Fig. 4h.

Crucially, both the forward and backward waves demonstrate nearly identical peak spectral strengths within the momentum gap, akin to the characteristics observed in the case of photonic time-crystals with extended temporal durations, as documented in[24].

FDTD simulation setup

In addition to the developed approach based on the temporal transfer matrix method, we also employed the finite difference time domain (FDTD) method to validate the obtained waveforms in Figs. 3 and 4. In the one-dimensional FDTD simulation, the Yee algorithm is employed alongside Perfectly Matched Layer (PML) absorbing boundary conditions.

The grid comprises 6799 points, each with a size of $\Delta z = \lambda/200$, where λ denotes the wavelength corresponding to the maximum frequency of interest. To ensure numerical stability, the Courant number (S_c) is set to unity, with $S_c = c\Delta t/\Delta z = 1$, where c represents the speed of light. There are 64 PML cells placed on both sides to terminate the grid. The excitation source is located at $200\Delta z$, and the probes are strategically positioned at $6686\Delta z$ and $114\Delta z$ to record transmission (forward-scattering) and reflection (backward-scattering) waves, respectively.

The permittivity (ε) of the medium is time-dependent, changing periodically between values ε_1 and ε_2 over a cycle T_p, while the nonmagnetic material with $\mu = \mu_o$ is considered. Both the initial and final states are characterized by $\varepsilon = \varepsilon_1$. The simulation spans 15,000 iterations, providing a comprehensive exploration of the dynamics of the electromagnetic field.

Table 1 presents the Root Mean Square (RMS) values for the differences between the waveforms obtained by the FDTD method and those derived from our approach, considering both forward- and backward-scattering waves for various values of N_c. Furthermore, the results obtained by both the FDTD method and the approach

	Fig. 3 (FW)	Fig. 4 (FW)	Fig. 3 (BW)	Fig. 4 (BW)
$N_c = 2$	6.38×10^{-3}	9.18×10^{-4}	5.24×10^{-4}	3.59×10^{-4}
$N_c = 4$	4.88×10^{-3}	4.14×10^{-3}	8.34×10^{-4}	2.79×10^{-3}
$N_c = 8$	8.18×10^{-3}	9.79×10^{-3}	6.97×10^{-4}	9.21×10^{-3}
$N_c = 16$	4.75×10^{-3}	4.55×10^{-2}	3.02×10^{-3}	4.36×10^{-2}

Table 1. The table presents the Root Mean Square (RMS) error between outcomes obtained from Finite Difference Time Domain (FDTD) simulations and the approach presented in this paper. The forward- and backward-scattering waveforms are individually labeled as FW and BW in the table.

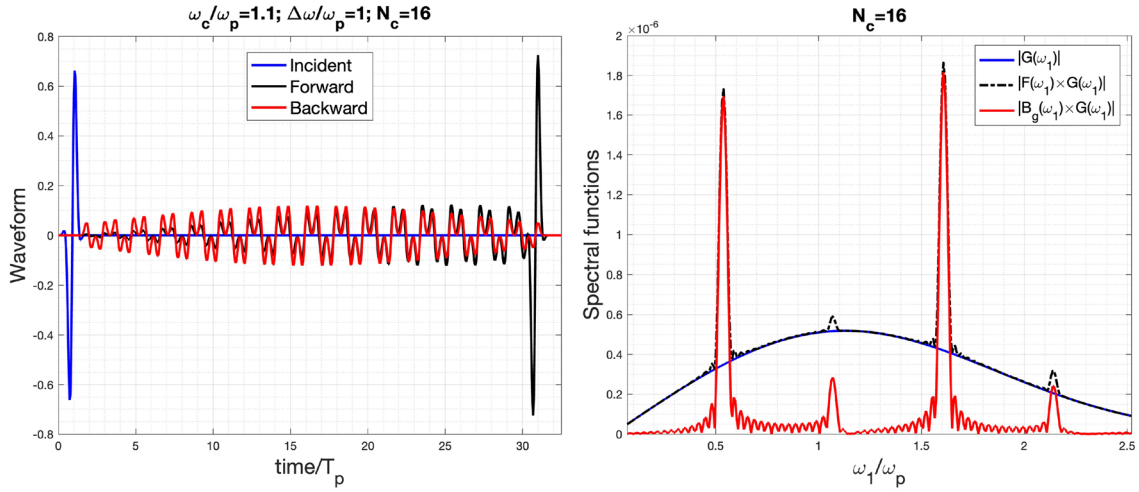

Figure 5. Incident, reflected and transmitted response for the case of $\omega_c/\omega_p = 1.1, d\omega/\omega_p = 1$ for $N_c = 16$ (**a**) time-domain waveform and (**b**) spectral function.

developed in this paper, along with their respective absolute differences, are plotted and shown in the Supplementary material.

Furthermore, Table 1 highlights a notable discrepancy between the results depicted in Fig. 3 obtained from the two approaches, particularly in the case of the forward-scattering wave. If we consider the transfer matrix approach as a more rigorous method, the observed deviation in the FDTD simulation might be attributed to the challenges associated with wide bandwidth operation. This significant deviation can be attributed to the fact that the segment of the narrow time pulse is being mimicked by the forward wave, copying the wide spectral response of the incident wave.

However, in the case of the backward wave, which only excites the wide pulse (or narrow spectral bandwidth) contributed by the complex ω_{eff} within the momentum gap, the error is relatively small compared to that of the forward waves. Additionally, noticeable RMS errors are observed in the cases of $N_c = 8$ and $N_c = 16$, indicating obvious parametric amplification.

The current example involves an ultra-wideband pulse incident into the temporal crystal. Notably, an ultrashort pulse can be employed to fully characterize linear photonic devices[44]. The central frequency is set at $\omega_c/\omega_p = 1.1$ with $d\omega/\omega_p = 1.0$. Figure 5a reveals that the initial segment of the forward wave replicates the incident pulse, albeit with minor amplitude deviations. This observation is supported by its spectral functions, as depicted in Fig. 5b. Evidently, the forward-wave spectrum encapsulates the profile of the incident wave.

Notably, the two oscillating modes characterized by larger imaginary parts of ω_{eff} (as depicted in Fig. 2) exhibit more pronounced spectral amplitudes within the forward and backward waves. This phenomenon becomes particularly evident in the extended tail featuring two distinct frequencies, which is clearly observable in Fig. 5a.

Furthermore, the RMS of the difference between the results obtained by the FDTD method and the approach employed in this paper has been calculated. The RMS of the differences is 1.76×10^{-2} for the forward propagating waveform and 4.24×10^{-3} for the backward propagating wave, respectively.

Interestingly, in the momentum gaps with a significant imaginary part of ω_{eff}, such as the first and third ones, the forward and backward waves almost have equal amplitudes. This is particularly evident in the cases with $N_c = 16$, as clearly observed in Figs. 3h, 4h, and 5b.

In the previously mentioned instances, the spectrum of the incident wave spans the momentum gaps. However, in the last example, where the central frequency and half-bandwidth are defined as $\omega_c/\omega_p = 0.3$ and $d\omega/\omega_p = 0.05$ respectively, it fails to encompass any momentum gaps. Notably, the forward wave replicates the incident waveform, as demonstrated in Fig. 6a. Additionally, the spectral functions of the incident and forward waves coincide, as depicted in Fig. 6b. The RMS value of the difference between the results of FDTD and this approach is 7.92×10^{-3} (for the forward-scattering wave) and 2.12×10^{-4} (for the backward-scattering wave), respectively.

Conclusion

In this study, we have developed a comprehensive mathematical framework and a rigorous formulation to analyze the waveforms of both forward and backward scattering within a photonic time-crystal with finite cycles (periods). The approach involves utilizing a cascade of temporal slabs based on the commonly used transfer matrix method to systematically establish the temporal input-output relationship for electric and magnetic field spectral functions in an environment that encompasses multiple temporal interfaces. Moreover, by incorporating the inverse fast Fourier transform, an efficient extraction of the corresponding time-domain waveforms can be achieved.

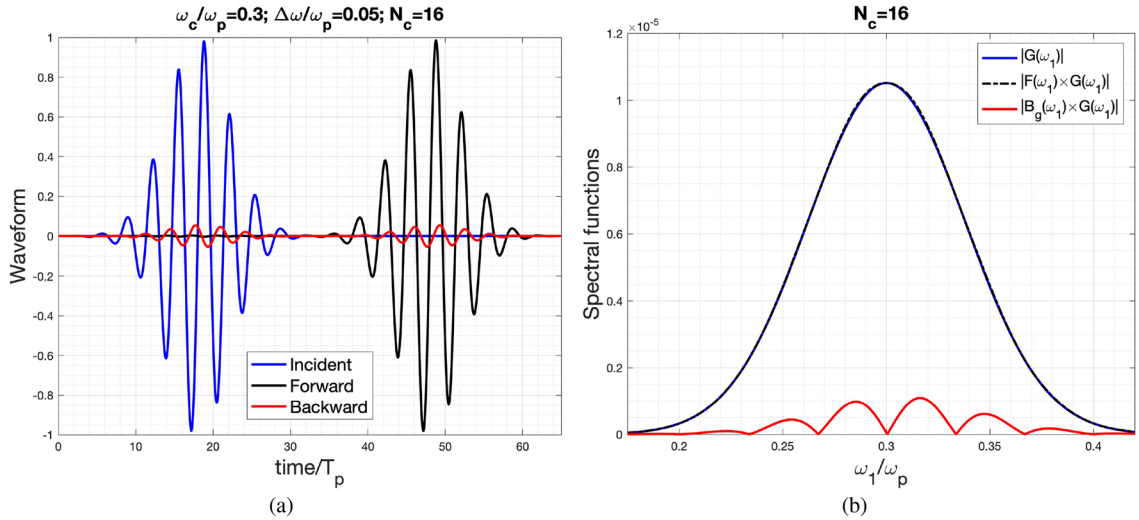

Figure 6. Waveform and Spectral functions of the Incident, reflected and transmitted waves for the case of $\omega_c/\omega_p = 0.3, d\omega/\omega_p = 0.05$ for $N_c = 16$. Subfigures (**a**) is the time-domain waveforms and (**b**) is the corresponding spectral functions.

It is noteworthy that this methodology distinguishes itself from the finite-difference time-domain (FDTD) method, offering a unique avenue for gaining deeper physical insights into the intricate dynamics of wave propagation through photonic time-crystals. Furthermore, the FDTD simulation has been employed to validate the analytical results.

The observations reveal that waveform shaping becomes evident when the spectrum of an incident wave covers the momentum gaps, with particularly distinct effects observed in instances characterized by a high number of cycles (N_c). Moreover, remarkable parametric amplification occurs when the incident spectrum is situated within the momentum gaps and spans extended cycles. Additionally, the introduction of extra modulated-Gaussian pulses takes place when an incident spectrum encompasses momentum gaps. This particular situation holds significant promise for applications in detecting mediums that display time-periodic changes in permittivity and permeability, especially within the domain of non-destructive testing.

Data availability

The data supporting the findings of this paper are available from the corresponding author upon reasonable request.

Received: 14 November 2023; Accepted: 31 January 2024
Published online: 04 February 2024

References

1. Morgenthaler, F. Velocity modulation of electromagnetic waves. *IRE Trans. Microw. Theor. Tech.* **6**, 167–172. https://doi.org/10.1109/TMTT.1958.1124533 (1958).
2. Holberg, D. & Kunz, K. Parametric properties of fields in a slab of time-varying permittivity. *IEEE Trans. Antennas Propag.* **14**, 183–194. https://doi.org/10.1109/TAP.1966.1138637 (1966).
3. Zurita-Sánchez, J. R., Halevi, P. & Cervantes-González, J. C. Reflection and transmission of a wave incident on a slab with a time-periodic dielectric function $\varepsilon(t)$. *Phys. Rev. A* **79**, 053821. https://doi.org/10.1103/PhysRevA.79.053821 (2009).
4. Martínez-Romero, J. S. & Halevi, P. Parametric resonances in a temporal photonic crystal slab. *Phys. Rev. A* **98**, 053852. https://doi.org/10.1103/PhysRevA.98.053852 (2018).
5. Zurita-Sánchez, J. R. & Halevi, P. Pulse propagation through a slab with time-periodic dielectric function ϵ(t). *Opt. Express* **20**, 5586–5600. https://doi.org/10.1364/OE.20.005586 (2012).
6. Cassedy, E. Temporal instabilities in traveling-wave parametric amplifiers (correspondence). *IRE Trans. Microw. Theor. Tech.* **10**, 86–87. https://doi.org/10.1109/TMTT.1962.1125452 (1962).
7. Cassedy, E. & Oliner, A. Dispersion relations in time-space periodic media: Part I-stable interactions. *Proc. IEEE* **51**, 1342–1359. https://doi.org/10.1109/PROC.1963.2566 (1963).
8. Cassedy, E. Dispersion relations in time-space periodic media part II-unstable interactions. *Proc. IEEE* **55**, 1154–1168. https://doi.org/10.1109/PROC.1967.5775 (1967).
9. Xiao, Y., Agrawal, G. P. & Maywar, D. N. Spectral and temporal changes of optical pulses propagating through time-varying linear media. *Opt. Lett.* **36**, 505–507. https://doi.org/10.1364/OL.36.000505 (2011).
10. Torrent, D. Strong spatial dispersion in time-modulated dielectric media. *Phys. Rev. B* **102**, 214202. https://doi.org/10.1103/PhysRevB.102.214202 (2020).
11. Xiao, Y., Maywar, D. N. & Agrawal, G. P. Reflection and transmission of electromagnetic waves at a temporal boundary. *Opt. Lett.* **39**, 574–577. https://doi.org/10.1364/OL.39.000574 (2014).
12. Bakunov, M. I. & Maslov, A. V. Reflection and transmission of electromagnetic waves at a temporal boundary: Comment. *Opt. Lett.* **39**, 6029–6029. https://doi.org/10.1364/OL.39.006029 (2014).
13. Mendonca, J. T. *Theory of Photon Acceleration* 1st edn. (CRC Press, 2000).
14. Gratus, J., Seviour, R., Kinsler, P. & Jaroszynski, D. A. Temporal boundaries in electromagnetic materials. *N. J. Phys.* **23**, 083032. https://doi.org/10.1088/1367-2630/ac1896 (2021).

15. Mendonça, J. T., Martins, A. M. & Guerreiro, A. Temporal beam splitter and temporal interference. *Phys. Rev. A* **68**, 043801. https://doi.org/10.1103/PhysRevA.68.043801 (2003).
16. Zhang, J., Donaldson, W. R. & Agrawal, G. P. Temporal reflection and refraction of optical pulses inside a dispersive medium: An analytic approach. *J. Opt. Soc. Am. B* **38**, 997–1003. https://doi.org/10.1364/JOSAB.416058 (2021).
17. Ramaccia, D., Alù, A., Toscano, A. & Bilotti, F. Temporal multilayer structures for designing higher-order transfer functions using time-varying metamaterials. *Appl. Phys. Lett.* **118**, 101901. https://doi.org/10.1063/5.0042567 (2021).
18. Pacheco-Peña, V. & Engheta, N. Antireflection temporal coatings. *Optica* **7**, 323–331. https://doi.org/10.1364/OPTICA.381175 (2020).
19. Ramaccia, D., Toscano, A. & Bilotti, F. Light propagation through metamaterial temporal slabs: Reflection, refraction, and special cases. *Opt. Lett.* **45**, 5836–5839. https://doi.org/10.1364/OL.402856 (2020).
20. Pacheco-Peña, V. & Engheta, N. Effective medium concept in temporal metamaterials. *Nanophotonics* **9**, 379–391. https://doi.org/10.1515/nanoph-2019-0305 (2020).
21. Stefanini, L. *et al.* Temporal interfaces by instantaneously varying boundary conditions. *Phys. Rev. B* **106**, 094312. https://doi.org/10.1103/PhysRevB.106.094312 (2022).
22. Li, H., Yin, S., Galiffi, E. & Alù, A. Temporal parity-time symmetry for extreme energy transformations. *Phys. Rev. Lett.* **127**, 153903. https://doi.org/10.1103/PhysRevLett.127.153903 (2021).
23. Zhang, J., Donaldson, W. R. & Agrawal, G. P. Time-domain Fabry–Perot resonators formed inside a dispersive medium. *J. Opt. Soc. Am. B* **38**, 2376–2382. https://doi.org/10.1364/JOSAB.428411 (2021).
24. Lustig, E., Sharabi, Y. & Segev, M. Topological aspects of photonic time crystals. *Optica* **5**, 1390–1395. https://doi.org/10.1364/OPTICA.5.001390 (2018).
25. Dikopoltsev, A. *et al.* Light emission by free electrons in photonic time-crystals. *Proc. Natl. Acad. Sci.* **119**, e2119705119. https://doi.org/10.1073/pnas.2119705119 (2022).
26. Biancalana, F., Amann, A., Uskov, A. V. & O'Reilly, E. P. Dynamics of light propagation in spatiotemporal dielectric structures. *Phys. Rev. E* **75**, 046607. https://doi.org/10.1103/PhysRevE.75.046607 (2007).
27. Taravati, S., Chamanara, N. & Caloz, C. Nonreciprocal electromagnetic scattering from a periodically space-time modulated slab and application to a quasisonic isolator. *Phys. Rev. B* **96**, 165144. https://doi.org/10.1103/PhysRevB.96.165144 (2017).
28. Rizza, C., Castaldi, G. & Galdi, V. Nonlocal effects in temporal metamaterials. *Nanophotonics* **11**, 1285–1295. https://doi.org/10.1515/nanoph-2021-0605 (2022).
29. Rizza, C., Castaldi, G. & Galdi, V. Short-pulsed metamaterials. *Phys. Rev. Lett.* **128**, 257402. https://doi.org/10.1103/PhysRevLett.128.257402 (2022).
30. Castaldi, G., Rizza, C., Engheta, N. & Galdi, V. Multiple actions of time-resolved short-pulsed metamaterials. *Appl. Phys. Lett.* **122**, 021701. https://doi.org/10.1063/5.0132554 (2023).
31. Reyes-Ayona, J. R. & Halevi, P. Observation of genuine wave vector (k or β) gap in a dynamic transmission line and temporal photonic crystals. *Appl. Phys. Lett.* **107**, 074101. https://doi.org/10.1063/1.4928659 (2015).
32. Reyes-Ayona, J. R. & Halevi, P. Electromagnetic wave propagation in an externally modulated low-pass transmission line. *IEEE Trans. Microw. Theor. Tech.* **64**, 3449–3459 (2016).
33. Wilczek, F. Quantum time crystals. *Phys. Rev. Lett.* **109**, 160401. https://doi.org/10.1103/PhysRevLett.109.160401 (2012).
34. Else, D. V., Bauer, B. & Nayak, C. Floquet time crystals. *Phys. Rev. Lett.* **117**, 090402. https://doi.org/10.1103/PhysRevLett.117.090402 (2016).
35. Peng, S. T., Tamir, T. & Bertoni, H. L. Theory of periodic dielect waveguides. *IEEE Trans. Microw. Theor. Tech.* **23**, 123–133 (1975).
36. Moharam, M. G. & Gaylord, T. K. Rigorous coupled-wave analysis of grating diffraction–e-mode polarization and losses. *J. Opt. Soc. Am.* **73**, 451–455. https://doi.org/10.1364/JOSA.73.000451 (1983).
37. Hwang, R.-B. *Periodic Structures: Mode-Matching Approach and Applications in Electromagnetic Engineering* 1st edn. (Wiley-IEEE, 2012).
38. Galiffi, E. *et al.* Photonics of time-varying media. *Adv. Photon.* **4**, 014002 (2022).
39. Yang, D., Xu, J. & Werner, D. H. A generalized temporal transfer matrix method and its application to modeling electromagnetic waves in time-varying chiral media. *Appl. Phys. Lett.* **122**, 251102. https://doi.org/10.1063/5.0146235 (2023).
40. Castaldi, G., Pacheco-Peña, V., Moccia, M., Engheta, N. & Galdi, V. Exploiting space-time duality in the synthesis of impedance transformers via temporal metamaterials. *Nanophotonics* **10**, 3687–3699. https://doi.org/10.1515/nanoph-2021-0231 (2021).
41. Xu, J., Mai, W. & Werner, D. H. Generalized temporal transfer matrix method: a systematic approach to solving electromagnetic wave scattering in temporally stratified structures. *Nanophotonics* **11**, 1309–1320. https://doi.org/10.1515/nanoph-2021-0715 (2022).
42. Lee, S. *et al.* Parametric oscillation of electromagnetic waves in momentum band gaps of a spatiotemporal crystal. *Photon. Res.* **9**, 142–150. https://doi.org/10.1364/PRJ.406215 (2021).
43. Koutserimpas, T. T. Parametric amplification interactions in time-periodic media: Coupled waves theory. *J. Opt. Soc. Am. B* **39**, 481–489. https://doi.org/10.1364/JOSAB.445176 (2022).
44. Kampfrath, T., Beggs, D. M., Krauss, T. F. & Kuipers, L. K. Complete response characterization of ultrafast linear photonic devices. *Opt. Lett.* **34**, 3418–3420. https://doi.org/10.1364/OL.34.003418 (2009).

Acknowledgements

This work was supported by the National Science and Technology Council (NSTC) of Taiwan under Grant NSTC 112-2221-E-A49-054-MY3.

Author contributions

R.B. completed all the research works and wrote the manuscript.

Competing interests

The author declares no competing interests.

Additional information

Supplementary Information The online version contains supplementary material available at https://doi.org/10.1038/s41598-024-53391-8.

Correspondence and requests for materials should be addressed to R.-B.H.